Nano Energy 64 (2019) 103942

Contents lists available at ScienceDirect

Nano Energy

journal homepage: www.elsevier.com/locate/nanoen

Full paper

# Tuning phase evolution of β-$MnO_2$ during microwave hydrothermal synthesis for high-performance aqueous Zn ion battery

Mingqiang Liu[1], Qinghe Zhao[1], Hao Liu[1], Jinglong Yang, Xin Chen, Luyi Yang, Yanhui Cui, Weiyuan Huang, Wenguang Zhao, Aoye Song, Yuetao Wang, Shouxiang Ding, Yongli Song, Guoyu Qian, Haibiao Chen, Feng Pan*

*School of Advanced Materials, Peking University, Shenzhen Graduate School, Shenzhen, 518055, People's Republic of China*

ARTICLE INFO

*Keywords:*
Aqueous Zn battery
β-$MnO_2$
Phase evolution
Electrochemistry

ABSTRACT

Mild aqueous Zn–$MnO_2$ battery attracts lots of attention in energy storage filed due to its low cost, high safety and environmental friendliness. To achieve high-performance in battery, phase evolution processes of $MnO_2$ during synthesis and electrochemical reactions need to be understood. Herein, the phase evolution during microwave hydrothermal and correlated battery performance of β-$MnO_2$ are studied. The results demonstrate a phase evolution mechanism from an initial mixture of vernadite, nsutite, and pyrolusite (β-$MnO_2$) to a final single β-$MnO_2$ phase, along with enhanced structure stability, increased Mn valence, and decreased BET surface area. It is found that only when microwave hydrothermal time (MHT) ≥ 120 min, β-$MnO_2$ showing both high capacity and excellent cycling performance can be obtained. β-$MnO_2$ prepared under a MHT of 120 min shows a high reversible capacity of 288 mA h $g^{-1}$ with a median voltage of 1.36 V vs. $Zn/Zn^{2+}$, and high capacity retentions of 91.8% after 200 cycles at 0.5C and 84.3% after 1000 cycles at 4C, respectively. In addition, the formation of inactive $ZnMn_2O_4$ during cycling is observed, which contributes to the capacity fading of β-$MnO_2$ after long-term cycling. This research makes a step forward to the practical application of Zn–$MnO_2$ batteries, and contributes to the large-scale energy storage field.

## 1. Introduction

The large-scale energy storage (LSES) devices for future homes and industries require cheap, environmentally friendliness, safe and high-performance batteries [1,2]. Recently, the research on aqueous Zn–$MnO_2$ battery using mild acidic electrolyte attracted lots of attention for LSES.[3] $MnO_2$ (α- [4–6], β- [7,8], γ- [9], δ- [10,11], spinel [12,13], and amorphous [14,15] has a high theoretical capacity of about 308 mAh $g^{-1}$, with a median voltage about 1.3–1.4 V vs. $Zn/Zn^{2+}$, which is among the best cathode materials for aqueous battery. Meanwhile, $MnO_2$ is also a high-performance pseudo-capacitive material, and can offer the advantages of both capacitor and battery [16–18]. During recent years, by tuning electrolyte composition [19,20] and membrane material [21,22], the cycling performance of Zn–$MnO_2$ batteries has been much improved. Thus, the mild aqueous Zn–$MnO_2$ batteries have shown great potential for LSES application, owing to its superior electrochemical property, low cost, high safety, as well as easy recycling.

To accelerate the commercialization of the aqueous Zn–$MnO_2$ batteries, rapid synthesis of high-performance $MnO_2$ cathode is one of the key issues. Compared with tradition hydrothermal method, microwave assisted hydrothermal has the advantages of fast heating speed, uniform heating without temperature gradient, etc. [23,24], making it a promising synthesis method for industrial production. Some results have been reported relating to the synthesis process and electrochemical properties of β-$MnO_2$. The result from Xue's group [24] indicates that by tuning the $MnCl_2$–$KMnO_4$ redox reaction system, the α-, β-, and γ-phase $MnO_2$ can be selectively prepared and used in lithium-ion batteries and super-capacitors. Tao's group [25] reported that the crystallization of β-$MnO_2$ nanorods proceeds through two steps during hydrothermal process: γ-$MnO_2$ forms first via a dissolution-recrystallization process and then transform topologically into β-$MnO_2$ with increasing temperature. Kim's group [7] found a Zn intercalation mechanism for the tunnel-type β-$MnO_2$ nanorods via a combination of solid solution and conversion reactions. Another $MnO_2$ phase evolution under a hydrothermal condition was reported by Iversen's group [26],

* Corresponding author.
*E-mail address:* panfeng@pkusz.edu.cn (F. Pan).
[1] Contribute equally.

https://doi.org/10.1016/j.nanoen.2019.103942
Received 29 June 2019; Received in revised form 17 July 2019; Accepted 25 July 2019
Available online 30 July 2019

involving initial formation of δ-$MnO_2$, then a transformation to α-$MnO_2$, and subsequently to β-$MnO_2$. However, the phase evolution of β-$MnO_2$ under a microwave hydrothermal condition is rarely studied, and the electrochemical property of β-$MnO_2$ and corresponding reaction mechanism are not clear. Besides, as a cathode material for aqueous Zn ion battery, a capacity activation and subsequent capacity fading process has been reported a lot [27–29], however, the fading mechanism of β-$MnO_2$ is far from clear.

In this study, we studied the phase evolution process and electrochemical properties of β-$MnO_2$ by tuning the microwave hydrothermal time (MHT). With increasing MHT, a transformation from a mixture of vernadite, nsutite, and pyrolusite to a single pyrolusite phase (β-$MnO_2$) has been observed. We found that only when MHT ≥120 min, β-$MnO_2$ with both high capacity and superior cycling property can be obtained. Moreover, the reaction and fading mechanisms of β-$MnO_2$ cathode during cycling was also analyzed. Our study on the phase evolution and electrochemical properties of β-$MnO_2$ provides a viable approach for the practical application of the reversible aqueous Zn–$MnO_2$ batteries.

## 2. Results

### 2.1. Phase evolution of β-$MnO_2$

The microwave assisted hydrothermal synthesis of β-$MnO_2$ was conducted at 180 °C, in which $MnSO_4$ and $(NH_4)_2S_2O_8$ were used as reducing agent and oxidant, respectively. XRD results of phase evolution of the products with increasing MHT are shown in Fig. 1a. When the MHT was less than 30 min, the product was a mixture of three phases, including nsutite (PDF#17–0510), vernadite (PDF#15–0604) and pyrolusite (PDF#72–1984, β-$MnO_2$). The corresponding XRD fitting of the product at 15 min is shown in Fig. S1a, and the corresponding microstructures of the three phases are shown from Figs. S1b–S1d. All the phases exhibit tunneled structure, i.e., 2 × 2 and 1 × 1 tunnels for vernadite, 1 × 3 and 1 × 1 tunnels for nsutite, and 1 × 1 tunnels for pyrolusite (β-$MnO_2$). When MHT ≥30 min, only β-$MnO_2$ with 1 × 1 tunnels can be observed. It is observed that the crystal structure of $MnO_2$ varies with increasing MHT from 30 to 120 min, and the main exposed surface of β-$MnO_2$ gradually changes from (101) to (110) plane. The $MnO_6$ octahedral arrangements on (110) and (101) planes are shown in Fig. S2. Compared with (101) plane, (110) plane presents lower surface energy (Table S1), which may be responsible for the transformation of the main exposed surface as MHT prolongs. After MHT exceeds 120 min, XRD pattern of β-$MnO_2$ stabilizes and remains the same. The detailed SEM morphological evolution of the product is shown in Fig. S3, showing a morphology transformation from a mixture of nanofibers and nanosheets to only nanofibers as the MHT increases.

To further identify the presence of three phases in the product at MHT of 15 min (M − 15), TEM and high-resolution TEM (HRTEM) images were also obtained. Fig. 1b shows that M − 15 is a mixture of nanosheets and nanofibers. HRTEM image of nanofiber (Fig. 1c) in region 1 shows a lattice fringes of 6.89 Å, which can be indexed to the (110) plane of vernadite. In region 2 (Fig. 1d), the lattice fringes of 2.44 Å is indexed to the (220) plane of nsutite. Fig. 1e shows the HRTEM images of nanofiber in region 3, and the lattice fringes of 1.56 Å can be indexed to the (220) plane of β-$MnO_2$. Thus, it can be confirmed that the product at 15 min is a mixture of vernadite, nsutite and pyrolusite phases based on the combined results of XRD and HRTEM. The β-$MnO_2$ at 120 min (M − 120) shows a single nanofiber morphology (Fig. 1f), and the corresponding HRTEM image (Fig. 1g) presents a lattice fringes of 3.15 Å, which is consistent with (110) plane of β-$MnO_2$. The FFT diffraction patterns in Fig. 1c, d, 1e and 1g are shown in Fig. S4. Thus, an asymptotic transformation process from a mixture of three manganese oxide phases to a single phase of β-$MnO_2$ is demonstrated.

Why the final product under the microwave hydrothermal condition in this study is β-$MnO_2$? This question can be answered by calculating the DFT relative energy of these three phases. During hydrothermal reaction, the solvent becomes acidic due to the formation of sulfuric acid by-products ($MnSO_4 + (NH_4)_2S_2O_8 + 2H_2O \rightarrow MnO_2 + (NH_4)_2SO_4 + 2H_2SO_4$). Consequently, some $H^+$ will be absorbed inside the tunnels of manganese oxides, forming Mn–O–H bonds, as shown in the subsequent XPS analysis in Fig. 2e. We assume that ~0.5 mol $H^+$ is adsorbed in ~1 mol $MnO_2$, and the corresponding DFT calculation results are shown in Table S2. The results indicate that the relative energy of β-$MnO_2$ with 1 × 1 tunnels is the lowest among three phases, namely, β-$MnO_2$ has the highest structural stability compared with vernadite and nsutite, which will also be confirmed by the subsequent TGA results in Fig. 2b.

To obtain more physical and chemical information of manganese oxides, FTIR, TGA, XPS and BET tests were conducted. FTIR results in Fig. 2a show that the characteristic absorption bands in the range of 400–800 $cm^{-1}$ and 3400-3500 $cm^{-1}$ are assigned to Mn–O stretching

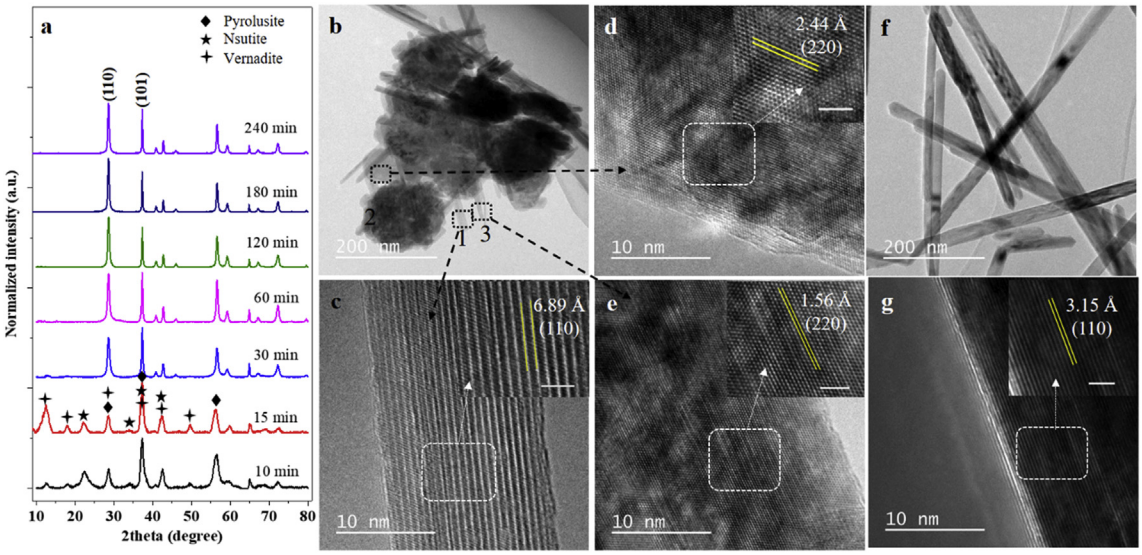


**Fig. 1.** Phase evolution of products with increasing MHT. (a) XRD patterns of products at different MHTs; (b) TEM image of product at 15 min, and corresponding HRTEM images of (c) vernadite, (d) nsutite, and (e) pyrolusite (β-$MnO_2$); (f) TEM image of product at 120 min, and corresponding (g) HRTEM image of β-$MnO_2$. Scale bars in insets of (c), (d), (e) and (g) are 2 nm.

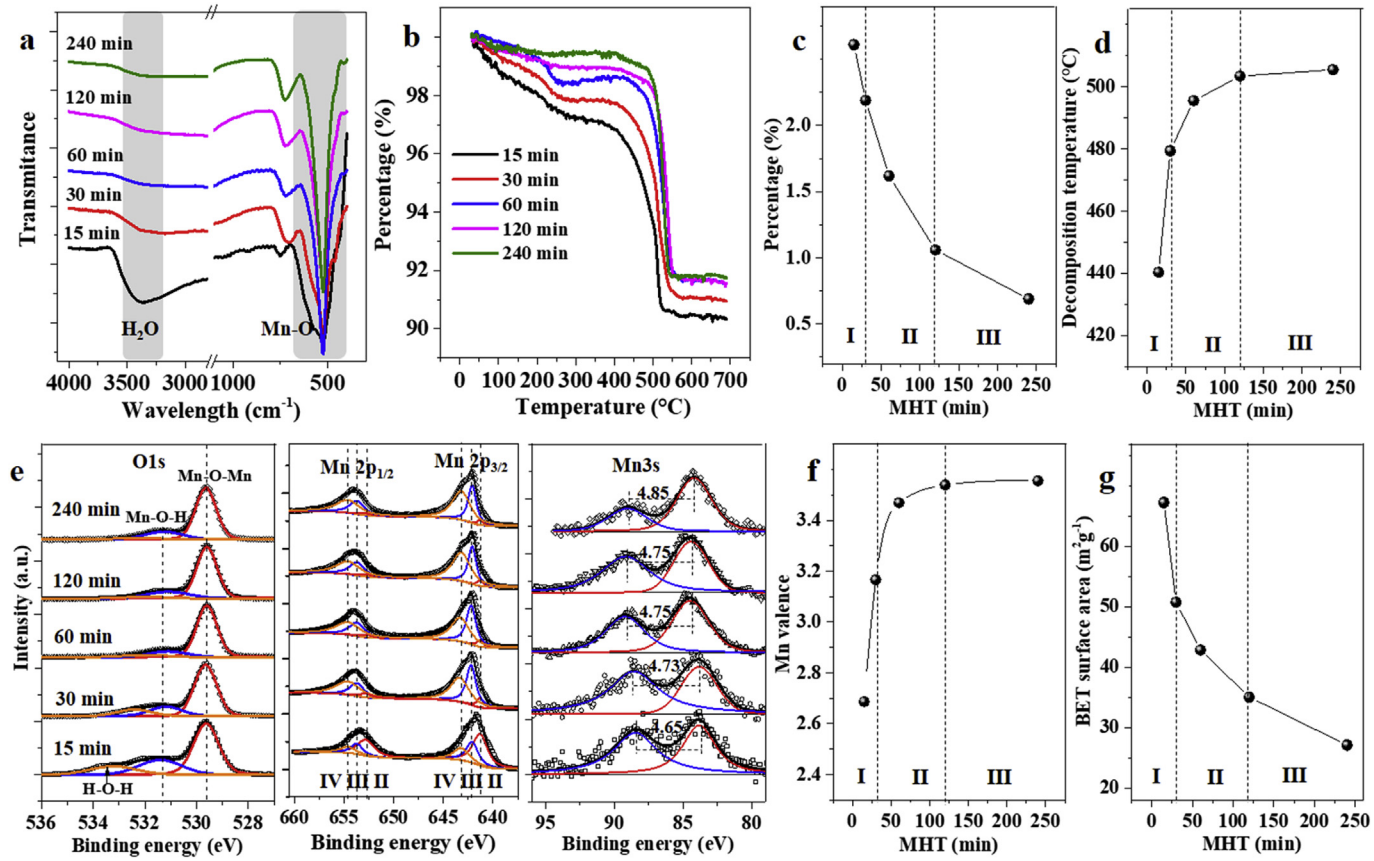


**Fig. 2.** FTIR, TGA and XPS analyses of the manganese oxides with different microwave hydrothermal times. (a) FTIR analysis, (b) TGA curves, and corresponding changing curves of (c) percentage of residual $H_2O$ and (d) decomposition temperature of manganese oxides; (e) XPS spectra of O 1s, Mn 2p, and Mn3s spectrums, the corresponding (f) Mn valence from Mn 2p analyses, and (g) BET surface areas.

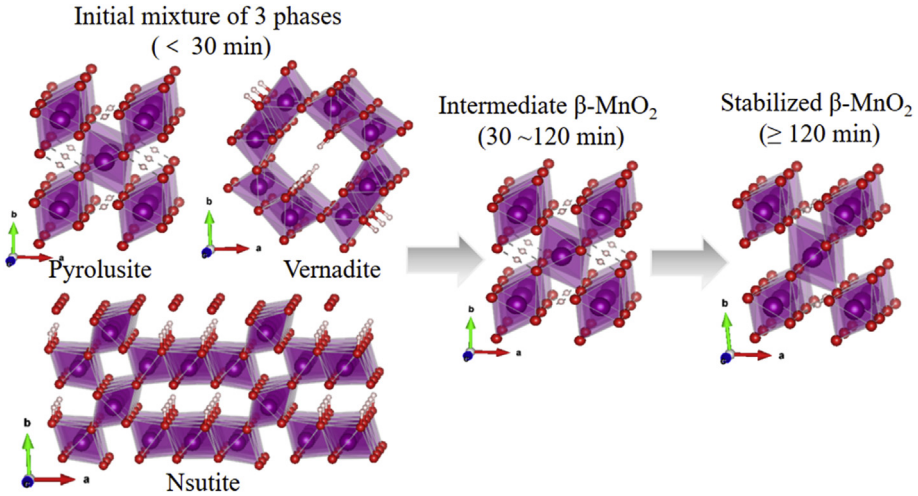


**Fig. 3.** Schematic representation of the microwave assisted phase evolution of manganese oxides.

vibrations of $MnO_6$ octahedra, and H–O–H stretching vibrations of residual $H_2O$, respectively [30]. As MHT increases, the absorption bands of H–O–H stretching vibration weakens, and the characteristic vibration peaks of $MnO_6$ octahedra become sharper, indicating a higher crystallinity of β-$MnO_2$. Fig. 2b shows the thermos gravimetric analysis (TGA) curves of the manganese oxides. Through analyzing the TGA data, the content of residual $H_2O$ in manganese oxides is obtained (Fig. 2c), which shows that the residual $H_2O$ decreases gradually with the increasing MHT. The diminish of vernadite and nsutite phases may be responsible for the decreased residual $H_2O$ content, because crystal $H_2O$ can be stored in the 2 × 2 and 1 × 3 tunnels, but not in the 1 × 1 tunnels [31]. In Fig. 2d, the decomposition temperature of the products ($3MnO_2 \rightarrow Mn_3O_4 + O_2$) increases rapidly before 120 min, indicating that the thermal stability of β-$MnO_2$ increases as MHT prolongs.

Fig. 2e shows the XPS spectra of O 1s, Mn 2p and Mn 3s at different MHTs. For O 1s, the bonding energy peaks of Mn–O–Mn, Mn–O–H and H–O–H can be identified. The presence of Mn–O–H bonds is associated with the $H^+$ adsorption in acidic electrolyte, and the diminish of H–O–H bonds with increasing MHT attributes to the disappearance of vernadite and nsutite, as well as the increasing crystallinity of

manganese oxides. The Mn $2p_{3/2}$ peaks can be divided into three peaks with binding energies of 641.3 eV (II), 642.2 eV (III) and 642.9 eV (IV), and the Mn $2p_{1/2}$ peak can also be divided into three peaks with binding energies of 652.8 eV (II), 653.7 eV (III) and 654.6 eV (IV) [32]. Based on Mn 2p results, the Mn valence is calculated and plotted in Fig. 2f. Mn valence of the products increases rapidly before 120 min, and then levels off after 120 min, where β-$MnO_2$ becomes stable. The energy separation for the Mn 3s spectra increases from 4.65 to 4.85 eV, which also indicates a higher Mn valence state with increasing MHT. In Fig. 2g, BET surface area gradually decreases with the increasing MHT, indicating a gradual crystallization process of β-$MnO_2$.

Based on above results, a phase evolution mechanism of β-$MnO_2$ can be proposed (Fig. 3) as follows: before 30 min, the product is a mixture of nsutite, vernadite and pyrolusite. From 30 to 120 min, only a single phase of intermediate β-$MnO_2$ can be observed, with lower Mn valence, lower structural stability and higher BET surface area compared with material after 120 min of MHT. When MHT ≥120 min, a stable β-$MnO_2$ with high Mn valence state, high structural stability and low BET surface area can be obtained.

### 2.2. Electrochemical performance

Fig. S5 and S6 compare the electrochemical performance of the products synthesized using different MHTs, and they show that the ideal MHT should be above 120 min to obtain a high-performance β-$MnO_2$ cathode material with both superior cycling performance and high discharge capacity. Based on this result, M − 120 was chosen for demonstrating the battery performance. Fig. 4a shows the galvanostatic charge/discharge profile of M − 120 at the rate of 0.05 C, where the achieved capacity is calculated by mass loading of active materials in electrodes (i.e. active loading of ~2.5 mg $cm^{-2}$). 3 M $ZnSO_4$ + 0.2 M $MnSO_4$ is used as electrolyte, and the pre-added $MnSO_4$ can effectively accommodate the dissolution equilibrium of $Mn^{2+}$ from $MnO_2$ electrode during discharging, which results in an enhanced cycling performance of β-$MnO_2$ (Fig. S7). A high reversible discharge capacity of ~288 mAh $g^{-1}$ was observed, with a median voltage of ~1.36 V vs. $Zn/Zn^{2+}$, which is very close to the theoretical capacity of β-$MnO_2$ (theoretical capacity of ~312 mAh $g^{-1}$, Fig. S8). Fig. 4b shows the cyclic voltammetry of M-120. An obvious cathodic peak around 1.21 V and a corresponding anodic peak around 1.58 V can be observed in the 1st cycle. In the 2nd cycle, the redox peak currents mentioned above decrease, and a new pairs of redox peaks emerge at 1.37 V and 1.63 V, respectively, indicating a two-step charge storage process.

Fig. 4c shows the rate performance of M − 120, and the corresponding charge/discharge profiles at different current densities are shown in Fig. 4d. As shown in Fig. 4c, the cell exhibits reversible discharge capacity of 285, 256, 221, 193, 179, and 156 mAh $g^{-1}$ at current densities of 0.1 C, 0.25 C, 0.5 C, 1 C, 2 C and 4 C, respectively, which is an excellent rate performance for aqueous Zn–$MnO_2$ batteries (Table S3). In addition, when returning back 0.1 C, the discharge capacity recovers to 282 mAh $g^{-1}$, showing a high reversibility of the M − 120 cathode. Notably, we also observed that the two discharge plateaus evolve to a single one as the rate is over 1C, which should be attributed to the $H^+$ insertion, which dominates the discharge process at high rates, and will be identified in the following section. Cycling stabilities of M − 120 at 0.5 C and 2 C were also evaluated, as shown in Fig. 4e and f. In Fig. 4e, M − 120 delivers an initial capacity of 218 mAh $g^{-1}$ at 0.5 C, with a Coulombic efficiency (CE) around 99% and capacity retention of 91.4% after 200 cycles. At current rate of 4 C, M − 120 delivers an initial capacity of 161 $mAhg^{-1}$, with a high CE approximately 100% and capacity retention of 83.2% after 1000 cycles (Fig. 4f). Notably, we observe that both cycling curves at 0.5 C and 4 C show an initial activation and subsequent fading process, which will be discussed in the following section. Beside, Fig. 4f also shows an initial decrease of capacity in the first 20 cycles, which may be related to the $Mn^{2+}$ dissolution process (Fig. S7). Thus, M − 120 is a capable cathode material for a Zn-ion aqueous battery, and will be promising for the application of large-scale energy storage devices.

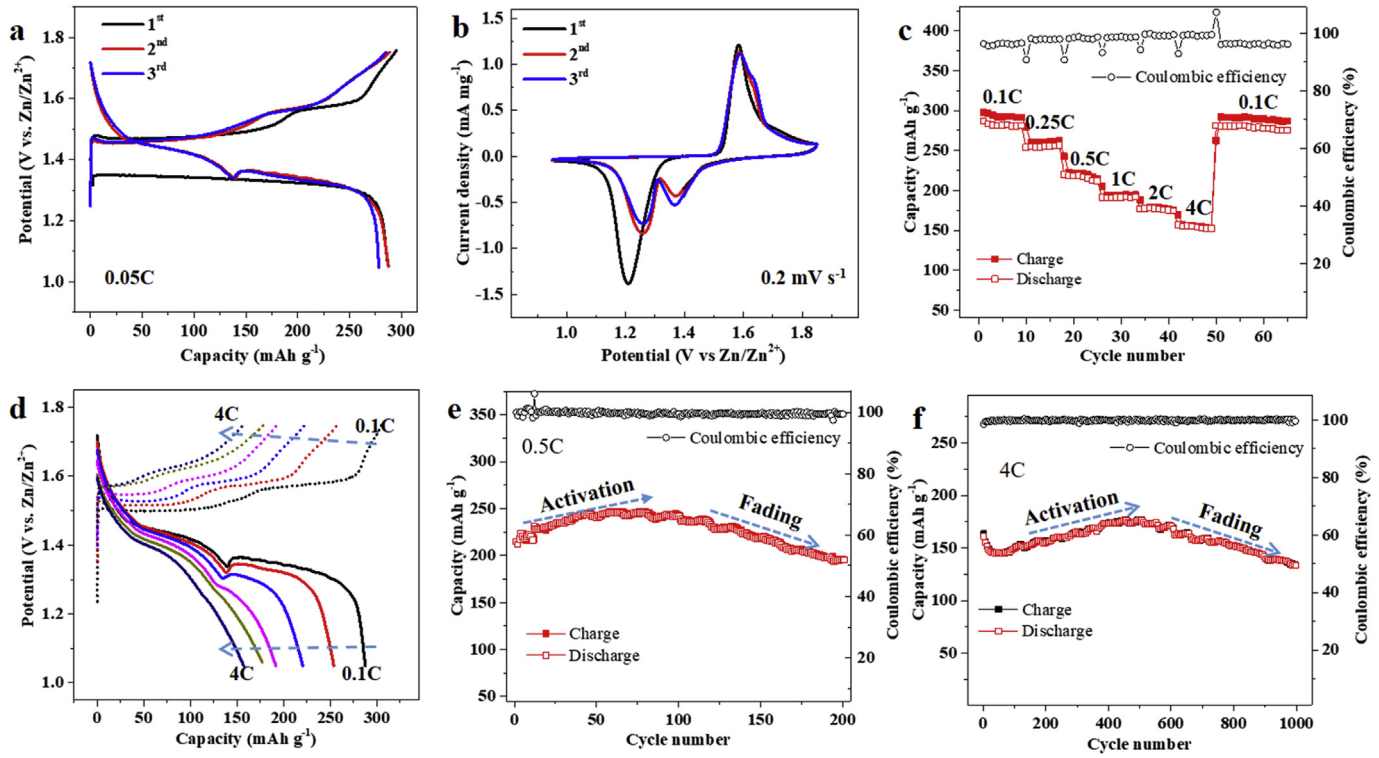


**Fig. 4.** Electrochemical performance of β-$MnO_2$ at 120 min. (a) galvanostatic discharge/charge curves at current of 0.05C; (b) CV curves of the 1st and 2nd cycle at scanning rate of 0.2 mV $s^{-1}$; (c) and (d) rate performance and corresponding charge/discharge curves at different current; cycling performance of (e) 200 cycles at 0.5 C, and (f) 1000 cycles at 4 C, both showing a capacity activation and subsequent fading process.

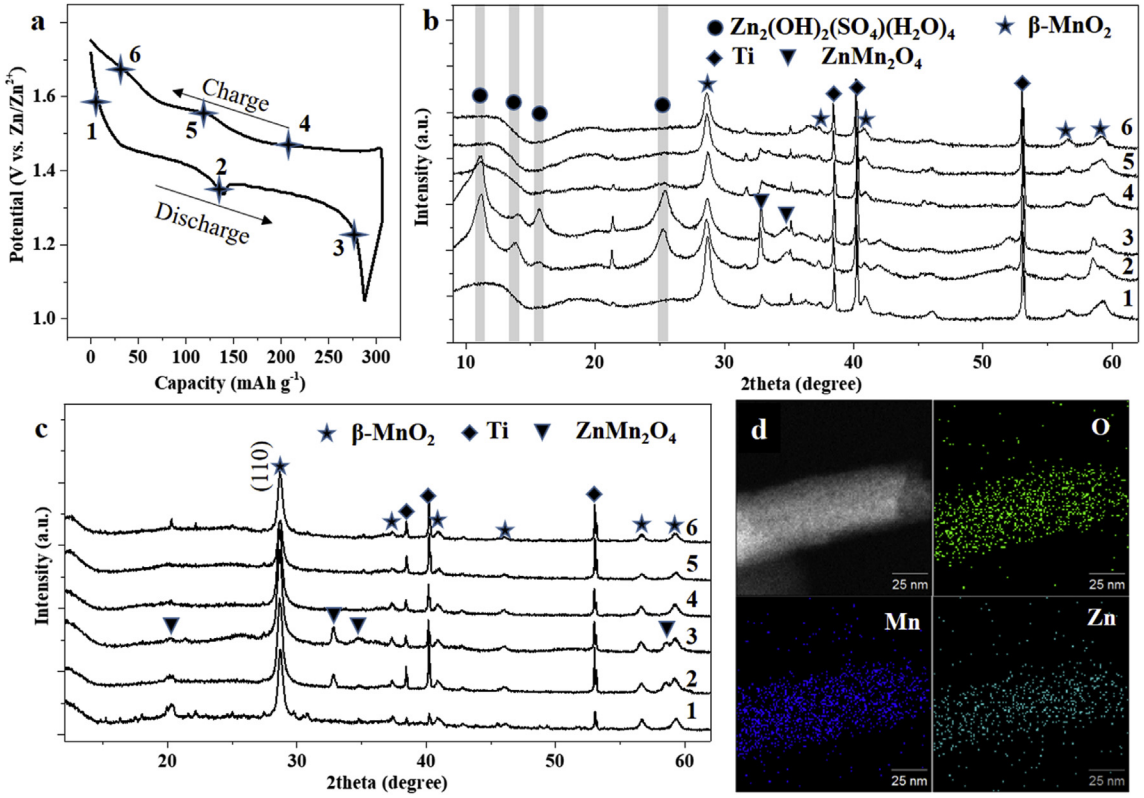


**Fig. 5.** (a) Galvanostatic charge/discharge profiles of β-$MnO_2$ cathode at current of 0.05C; (b) ex situ XRD profiles of electrodes at charge/discharge states from 1 to 6, showing a reversible $H^+$ insertion/extraction process, and (c) corresponding XRD profiles after immersed in a 10 vol% acetic acid; (d) EDS-mapping results of the β-$MnO_2$ electrode at discharge state 3, showing a successful Zn insertion during discharge process.

### 2.3. Reaction and fading mechanisms

In order to investigate the reaction and fading mechanisms of M − 120 upon cycling, XRD, XPS and TEM analyses were performed. Fig. 5a illustrates that six samples were taken from the 2nd discharge/charge cycle, and corresponding XRD patterns of electrodes in 3 M $ZnSO_4$ + 0.2 M $MnSO_4$ electrolyte are shown in Fig. 5b. During the discharge process, obvious peaks locating at around 11.1°, 14.0°, 15.6° and 25.3° emerged on surface of discharged electrodes of #2 and #3, which is related to the formation of $Zn_2(OH)_2(SO_4)(H_2O)_4$ (zinc sulfate hydroxide hydrate, ZSHH, PDF#09–0204). In the subsequent charge process (sample #4 to #6), the these ZSHH peaks decreases rapidly, and the XRD finally recover to the original pattern of β-$MnO_2$ cathode, indicating a good reversibility of the electrode reaction. The formation of ZSHH is attributed to the increasing concentration of $OH^-$ in electrode/electrolyte interface due to the consumption of $H^+$ in the electrolyte during discharge process, which is consistent with the report by Liu's group [8]. SEM was applied to visualize the morphologic evolution of β-$MnO_2$ electrode, and we observed that the flake-like products emerged during discharging, and then vanished during subsequent charging (Fig. S9). This highly reversible morphologic changes are consistent with the evolution observed in XRD results. Thus, $H^+$ insertion contributes to one part of the capacity of β-$MnO_2$ cathode.

Additionally, to eliminate the influence of ZSHH, we removed it by immersing the discharged electrodes in a 10 vol% acetic acid aqueous solution, and the obtained XRD patterns are shown in Fig. 5c. From Fig. 5c, some peaks located at 20.2°, 32.8°, 34.8° and 58.6° can be observed on discharged electrodes of #2 and #3, and these peaks are indexed to $ZnMn_2O_4$ (Hetaerolite, PDF#71–2499). TEM-mapping results in Fig. 5d indicates a successful $Zn^{2+}$ insertion into β-$MnO_2$ cathode at discharged electrode #3, which is consistent with the formation of $ZnMn_2O_4$. After recharged to 1.75 V (electrode #6), $Zn^{2+}$ was successfully extracted from the β-$MnO_2$ cathode (Fig. S10). Besides, we also observed that the peaks of (110) plane (~28.7°) of β-$MnO_2$ cathode changed slightly upon the $Zn^{2+}/H^+$ insertion/extraction process, which may indicate that $H^+$ insertion contributes to a major part of the capacity of M − 120, and the volumetric change of the crystal cell induced by $H^+$ insertion is small. Furthermore, $Zn^{2+}$ insertion can result in the conversion from tunneled β-$MnO_2$ to spinel-type $ZnMn_2O_4$. Thus, for β-$MnO_2$ cathode, a $Zn^{2+}/H^+$ co-insertion process during discharging is proposed, and part of β-$MnO_2$ can convert to spinel-type $ZnMn_2O_4$ during discharging, rather than the generation of layer-type Zn-buserite for a α-$MnO_2$ cathode [20,33]. The co-insertion of $Zn^{2+}$ and $H^+$ is responsible for the high capacity delivery (~288 mAh $g^{-1}$ at 0.05 C) of β-$MnO_2$, and $H^+$ insertion contributes to the high rate performance at a high current of 4 C. Besides, the CV curves at different scan rates are also conducted (Fig. S11), showing a solid diffusion controlled kinetics of $H^+$ and $Zn^{2+}$ of β-$MnO_2$ during charge/discharge cycles.

We also compared the XRD patterns of the cycled β-$MnO_2$ cathode to explain its fading mechanism. Fig. 6a shows the XRD patterns of pristine M − 120 electrode, fully charged electrode after 5 cycles at 0.05C, and fully charged electrode after 200 cycles at 0.5 C. Characteristic peaks of β-$MnO_2$ and $ZnMn_2O_4$ can be observed, and the detailed fitting of $ZnMn_2O_4$ product is shown in Fig. S12. After 200 cycles at 1 C, the characteristic peaks of $ZnMn_2O_4$ is obvious in the fully charged β-$MnO_2$ cathode. Mn 3s and Zn 2p spectra in Fig. 6b and c shows that $Zn^{2+}$ partially remains within the fully charged cathode, in the form of spinel $ZnMn_2O_4$.

SEM and TEM were also applied to further confirm the existence of $ZnMn_2O_4$. Some nanofibers with very rough surfaces can be observed in the fully charged β-$MnO_2$ electrode after 200 cycles at 0.5C (Fig. 6d). Fig. 6e shows the TEM morphology of the nanofiber in Fig. 6d, some cotton-like products (circled by white dotted lines) are observed

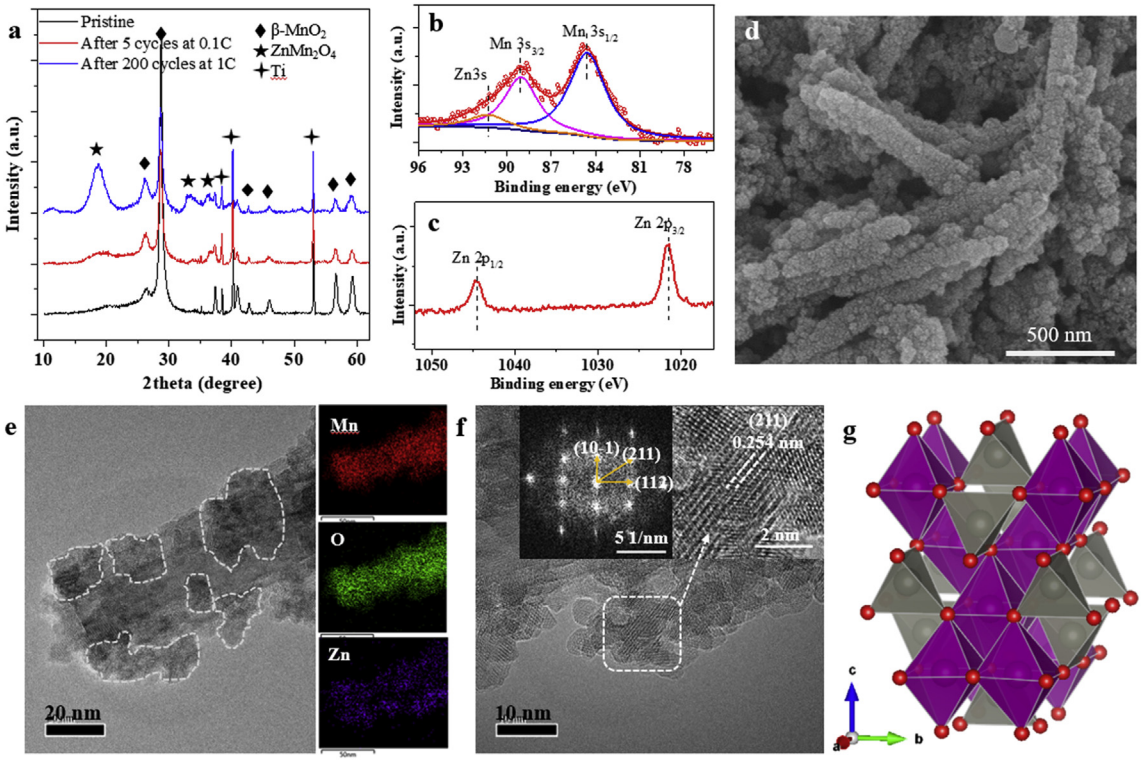


**Fig. 6.** (a) XRD patterns of pristine, fully charged electrodes after 5 cycles at 0.05C and 200 cycles at 1C; (b) Mn3s and (c) Zn2p spectrums for fully charged electrode after 200 cycles at current of 1C, and corresponding (d) SEM morphology, (f) TEM morphology and element mapping of Mn, O and Zn for β-$MnO_2$ nanofiber, (g) HRTEM image (Inset: FFT pattern) and (h) schematic of hetaerolite structure.

distributing on the surface of the β-$MnO_2$ nanofiber, which is consistent with the SEM result in Fig. 6d. The TEM results of EDS-mapping of Mn, O and Zn are also shown in Fig. 6e, it can be observed that Mn and O distribute uniformly throughout the nanofiber, while Zn can only be seen in the region of cotton-like products, indicating that the residual Zn only exists in the cotton-like products. HRTEM image of the cotton-like products are shown in Fig. 6f, a lattice fringe of 0.254 nm is assigned to the (211) plane of $ZnMn_2O_4$, the corresponding diffraction pattern also indicate the diffraction spots of (10-1), (112) and (211) planes, and schematic representation of crystal structure of $ZnMn_2O_4$ is shown in Fig. 6g. Thus, combining all the results of XRD, XPS, SEM and TEM, we can conclude that some $ZnMn_2O_4$ remains in the charged electrodes after long-term cycle, resulting in the capacity fading of M − 120 cathode.

To prove the hypothesis that "the generation of $ZnMn_2O_4$ is the main reason for the capacity fading issue" in Fig. 4e and f, we synthesized a spinel-type $ZnMn_2O_4$ as a cathode material for Zn ion battery (Fig. S13). The results show that $ZnMn_2O_4$ can only deliver an ultralow discharge capacity of ~32.6 mAh $g^{-1}$ at a current rate of 0.05 C, which is an order of magnitude lower than that of the β-$MnO_2$ cathode (288 mAh $g^{-1}$ at 0.05C). That is to say, after long-term discharge/charge cycle, part of the Mn in β-$MnO_2$ cathode will convert into the inactive $ZnMn_2O_4$, resulting in an irreversible capacity decay of Zn–$MnO_2$ batteries. Thus, the key to further improve the electrochemical property of β-$MnO_2$ cathode is to depress the formation of $ZnMn_2O_4$ during cycling, which need to be further investigated in the future.

## 3. Conclusion

In conclusion, the phase evolution mechanism, electrochemical property and reaction mechanism of β-$MnO_2$ prepared by microwave hydrothermal method were investigated. We revealed a phase transformation mechanism from an initial mixture of vernadite, nsutite, and pyrolusite to a final pure pyrolusite as the MHT increases. When MHT ≥120 min, the obtained β-$MnO_2$ is thermodynamically stable. The electrochemical property of β-$MnO_2$ cathode under MHT of 120 min was studied, showing both high capacity delivery of ~288 mAh $g^{-1}$ at 0.05 C, and high cycling stability with capacity retentions of 91.8% after 200 cycles at 0.5 C and 84.3% after 1000 cycles at 2 C. Furthermore, the capacity fading of β-$MnO_2$ cathode is mainly due to the formation of inactive $ZnMn_2O_4$ after long-term charge/discharge cycling. The present β-$MnO_2$ holds great promise for practical use of a high-performance aqueous Zn–$MnO_2$ batteries in large-scale energy storage, in view of superior battery performance, low cost, high safety, and environmental friendliness.

## 4. Experimental section

### 4.1. Synthesis of β-$MnO_2$

The synthesis process of β-$MnO_2$ is described as follows: 0.2 g glucose ($C_6H_{12}O_6{\cdot}H_2O$) and 2.70 g manganese sulfate monohydrate ($MnSO_4{\cdot}H_2O$) were dissolved into 40 mL deionized water under stirring (solution A). Second, 3.64 g ammonium persulfate ($(NH_4)_2S_2O_8$) was dissolved in 40 mL deionized water under stirring for 1 h (solution B). Then, the two solutions of A and B were mixed and stirred for 30 min. After stirring, the obtained solution was transferred into a 50 mL microwave hydrothermal device and heated at 180 °C for 10, 15, 30, 60, 120, 180, and 240 min, respectively. After hydrothermal treatment, the solution was filtered to collect the product. The product was then washed with deionized water and ethanol for 3 times, and dried in the vacuum oven at 100 °C overnight.

### 4.2. Materials characterizations

X-ray diffractometer (XRD, Bruker D8 ADVANCE) using Cu Kα radiation was used to characterize the crystal structure. Scanning electron

microscopy (SEM, JEOL JSM-7100 F) was used to observe the micro-morphology. The transmission electron microscopy (TEM, Titan G2 60–300, FEI) was used to characterize the morphology and selected-area electron diffraction (SAED) patterns. X-ray photoelectron spectroscopy (XPS, ESCALAB 250) was used to explore the electronic structure and compositional information. Nitrogen adsorption tests at 77 K using a Micromeritics Tristar II 3020 instrument was applied to measure the BET surface area. Thermogravimetry measurements (TGA, SII STA7300 analyzer) were performed under nitrogen atmosphere to illustrate the $H_2O$ content and decomposition temperature.

### 4.3. DFT calculation method

All calculations were performed using the plane-wave projector-augmented wave method [34] with an energy cut-off of 520 eV, as implemented in the Vienna ab initio simulation package (VASP) [35,36]. The Perdew-Burke-Ernzerhof (PBE) form of generalized gradient approximation (GGA) [37] was chosen as the exchange-correlation potential. The PBE + U approach was employed to take account of the short on-site Coulomb interaction (U) presented in the localized 3d electrons of Mn, with the U values set to 3.9 eV following the literature value [38]. The structures were relaxed until the forces were less than 0.03 eV/Å, and the energy convergent standard was $10^{-5}$ eV. The Monkhorst−Pack mesh [39,40] of unit cells was set to 6 × 6 × 9, 3 × 8 × 10, and 3 × 3 × 10 for manganese oxides with 1 × 1 tunnels, 1 × 3 tunnels, and 2 × 2 tunnels, respectively.

### 4.4. Electrochemical measurement

Electrochemical properties were tested using CR2032 coin-type cells. The working electrode was fabricated by blending active material, acetylene black (AB), and polyvinylidene fluoride (PVDF) in a weight ratio of 8:1:1 with N-methyl-2-pyrrolidone as solvent. The obtained slurry was casted onto a Ti foil (~10 μm) and vacuum-dried at 110 °C for 12 h. The loading mass of active material was 2.5–3.0 mg $cm^{-2}$. Glass fiber membrane and zinc foil were employed as the separator and anode, respectively. Aqueous solution containing 3 M $ZnSO_4$ and 0.2 M $MnSO_4$ was used as electrolyte. The assembled cells were galvanostatically cycled between 1.0 and 1.8 V using the LAND-CT2001A battery-testing instrument. Calculation of specific capacities was based on the mass of initial active materials. CVs were measured on a Chi 660e electrochemical workstation (CH Instruments Inc.).

## Author contributions

Mingqiang Liu, Qinghe Zhao and Hao Liu contributed equally to this work.

## Additional information

Experimental details and data are available in Supporting Information.

## Acknowledgement

This work was financially supported by National Key R&D Program of China (2016YFB0700600), Soft Science Research Project of Guangdong Province (No. 2017B030301013), and Shenzhen Science and Technology Research Grant (ZDSYS201707281026184).

## Appendix A. Supplementary data

Supplementary data to this article can be found online at https://doi.org/10.1016/j.nanoen.2019.103942.

## References

[1] T.M. Gür, Energy Environ. Sci. 11 (2018) 2696.
[2] Ming Song, Hua Tan, Dongliang Chao, Hong Jin Fan, Adv. Funct. Mater. 28 (2018) 1802564.
[3] Chang Zhang, Yaqiong Yang, Minxia Li, Xiaowei Wang, Yuping Wu, J. Mater. Chem. 2 (2014) 10739–10755.
[4] J. Matthias, A.M.H. Young, Steven M. George, Charles B. Musgrave, Chem. Mater. 27 (2015) 1172–1180.
[5] Boeun Lee, Hae Ri Lee, Haesik Kim, Kyung Yoon Chung, Byung Won Cho, Si Hyoung Oh, Chem. Commun. 51 (2015) 9265–9268.
[6] Xiulan Hu, Shoufeng Zhu, Huihong Huang, Jianbo Zhang, Yanqiu Xu, J. Cryst. Growth 434 (2016) 7–12.
[7] S. Islam, M.H. Alfaruqi, V. Mathew, J. Song, S. Kim, S. Kim, J. Jo, J.P. Baboo, D.T. Pham, D.Y. Putro, Y.K. Sun, J. Kim, J. Mater. Chem. 5 (2017) 23299–23309.
[8] H. Pan, Y. Shao, P. Yan, Y. Cheng, K.S. Han, Z. Nie, C. Wang, J. Yang, X. Li, P. Bhattacharya, Nat. Energy 1 (2016) 16039.
[9] M.H. Alfaruqi, M. Vinod, G. Jihyeon, S. Kim, J. Song, J.P. Baboo, H.C. Sun, J. Kim, Chem. Mater. 27 (2015) 3609–3620.
[10] S.D. Han, S. Kim, D. Li, V. Petkov, H.D. Yoo, P.J. Phillips, H. Wang, J.J. Kim, K.L. More, B. Key, R.F. Klie, J. Cabana, V.R. Stamenkovic, T.T. Fister, N.M. Markovic, A.K. Burrell, S. Tepavcevic, J.T. Vaughey, Chem. Mater. 29 (2017) 4874–4884.
[11] X. Peng, Y. Guo, Q. Yin, J. Wu, J. Zhao, C. Wang, S. Tao, W. Chu, C. Wu, Y. Xie, J. Am. Chem. Soc. 139 (2017) 5242–5248.
[12] N. Zhang, F. Cheng, Y. Liu, Q. Zhao, K. Lei, C. Chen, X. Liu, J. Chen, J. Am. Chem. Soc. 138 (2016) 12894.
[13] K. Shimokawa, T. Atsumi, M. Harada, R.E. Ward, M. Nakayama, Y. Kumagai, F. Oba, N.L. Okamoto, K. Kanamuraf, T. Ichitsubo, J. Mater. Chem. 7 (2019) 12225–12235.
[14] Y.Z. Zeng, X. Zhang Y. Meng, M. Yu, J. Yi, Y. Wu, X. Lu, Y. Tong, Adv. Mater. 29 (2017) 1700274.
[15] W. Sun, F. Wang, S. Hou, C. Yang, X. Fan, Z. Ma, T. Gao, F. Han, R. Hu, M. Zhu, J. Am. Chem. Soc. 139 (2017) 9775.
[16] H. Jia, Y. Cai, X. Zheng, J. Lin, H. Liang, J. Qi, J. Cao, J. Feng, W. Fei, ACS Appl. Mater. Interfaces 10 (2018) 38963–38969.
[17] Z. Hu, X. Xiao, C. Chen, T. Li, L. Huang, C. Zhang, J. Su, L. Miao, J. Jiang, Y. Zhang, J. Zhou, Nano Energy 11 (2015) 226–234.
[18] L. Sheng, L. Jiang, T. Wei, Z. Fan, Small 12 (2016) 5217–5227.
[19] J. Zhao, J. Zhang, W. Yang, B. Chen, Z. Zhao, d, H. Qiu, S. Dong, X. Zhou, G. Cui, L. Chen, Nano Energy 57 (2019) 625–634.
[20] N. Zhang, F. Cheng, J. Liu, L. Wang, X. Long, X. Liu, F. Li, J. Chen, Nat. Commun. 8 (2017) 405.
[21] Z. Wang, J. Hu, L. Han, Z. Wang, H. Wang, Q. Zhao, J. Liu, F. Pan, Nano Energy 56 (2019) 92–99.
[22] H. Li, C. Han, Y. Huang, Y. Huang, M. Zhu, Z. Pei, Q. Xue, Z. Wang, Z. Liu, Z. Tang, Y. Wang, F. Kang, B. Li, C. Zhi, Energy Environ. Sci. 11 (2018) 941.
[23] P. Wang, Y.J. Zhao, L. Wen, J. Chen, Z. Lei, Ind. Eng. Chem. Res. 53 (2014) 20116–20123.
[24] K. Chen, Y.D. Noh, K. Li, S. Komarneni, D. Xue, J. Phys. Chem. C 117 (2013) 10770–10779.
[25] G. Tao, F. Helmer, N. Poul, Nanotechnology 20 (2009) 055610.
[26] S. Birgisson, D. Saha, B.B. Iversen, Cryst. Growth Des. 18 (2018) 827–838.
[27] B. Wu, G. Zhang, M. Yan, T. Xiong, P. He, L. He, X. Xu, L. Mai, Small 14 (2018) 1703850.
[28] Y. Huang, J. Liu, Q. Huang, Z. Zheng, P. Hiralal, F. Zheng, D. Ozgit, S. Su, S. Chen, P.H. Tan, npj Flex. Electron. 21 (2018) 6.
[29] Y. Li, S. Wang, J.R. Salvador, J. Wu, B. Liu, W. Yang, J. Yang, W. Zhang, J. Liu, J. Yang, Chem. Mater. 31 (2019) 2036–2047.
[30] J. Huang, Z. Wang, M. Hou, Nat. Commun. 9 (2018) 2906.
[31] Y. Yuan, C. Zhan, K. He, H. Chen, W. Yao, S. Sharifiasl, B. Song, Z. Yang, A. Nie, X. Luo, Nat. Commun. 7 (2016) 13374.
[32] H. Jiang, Z. Wei, L. Ma, Y. Yuan, J.J. Hong, X. Wu, D.P. Leonard, J. Holoubek, J.J. Razink, W.F. Stickle, F. Du, T. Wu, J. Lu, X. Jia, Angew. Chem. Int. Ed. 58 (2018) 5286–5291.
[33] B. Lee, S.Y. Chong, H.R. Lee, K.Y. Chung, B.W. Cho, H.O. Si, Sci. Rep. 4 (2014) 6066.
[34] G. Kresse, Phys. Rev. B 53 (1999) 1758–1775.
[35] G. Kresse, J. Furthmüller, Comput. Mater. Sci.. 6 (1996) 15–50.
[36] G. Kresse, J. Furthmüller, Phys. Rev. B 54 (1996) 11169–11186.
[37] J.P. Perdew, M. Ernzerhof, K. Burke, J. Chem. Phys. 105 (1996) 9982–9985.
[38] S.L. Dudarev, G.A. Botton, S.Y. Savrasov, C.J. Humphreys, A.P. Sutton, Phys. Rev. B 57 (1998) 1505–1509.
[39] H.J. Monkhorst, Phys. Rev. B 16 (1976) 1748–1749.
[40] R. Wang, G.Y. Qian, T.C. Liu, M.F. Li, J.J. Liu, B.K. Zhang, W.M. Zhu, S.K. Li, W.G. Zhao, W.Y. Yang, X.B. Ma, Z.D. Fu, Y.T. Liu, J.B. Yang, L. Jin, Y.G. Xiao, F. Pan, Nano Energy 62 (2019) 709–717.

**Mingqiang Liu** got his bachelor's degree from the school of Chemistry, Jilin university in 2016. He is now studying at the School of Advanced Materials, Peking university Shenzhen graduate school. His research interest majors in the cathode materials for aqueous Zn ion batteries, and Lithium ion batteries.

**Qinghe Zhao** received his B.S. degree from University of Science and Technology of Beijing (USTB, China) in 2010, and earned Ph.D. degree from the School of Advanced Materials at USTB in 2016, majoring in the electrochemical corrosion behavior of iron-based alloys, under the supervision of Prof. Minxu Lu. Dr. Zhao is now associate researcher in School of Advanced Materials, Peking University Shenzhen Graduate School, China. His research interests mainly focus on the key materials and technologies for energy storage and conversion applications, including electro-catalyst, zinc ion and sodium ion batteries.

**Hao Liu** received his B.S. degree from the School of Electronic Science and Engineering at JiLin University (JLU, China). Now he is studying at the School of Advanced Materials, Peking University Shenzhen Graduate School to get a master's degree under the supervision of Prof. Feng Pan. His research interests include understanding the mechanism inside the lithium-oxygen batteries and zinc ion batteries.

**Jinlong Yang** received his Ph.D. degree in 2014 from Wuhan University of Technology. He was a postdoctoral fellow from 2014 to 2018 at School of Advanced Materials, Peking University, Shenzhen Graduate School, China. In 2018, he joined Stanford University, USA as a postdoctoral visiting scholar, His research interests include: energy materials (battery and catalysis), nanotechnology and electrochemistry.

**Xin Chen** is currently a postgraduate student in Prof. Feng Pan's group at the School of Advanced Materials, Peking University, Shenzhen Graduate School. He received his B.S. in School of Materials Science and Engineering, Central South University, China.His research mainly focuses on theoretical calculation and design of advanced materials.

**Luyi Yang** received his Ph.D. degree from the School of Chemistry at Southampton University in 2015 under the supervision of Prof. John Owen. Dr. Yang is currently a associate researcher at the School of Advanced Materials, Peking University Shenzhen Graduate School. His research interests mainly focus on designing key components for solid-state batteries.

**Yanhui Cui** received his B.E. degree in Packing Engineering from Zhengzhou University, China in 2010. After which he completed his Master and Ph.D degree under the supervision of Prof. Andrew Baker and Junwei Wu in Materials Science at Harbin Institute of Technology (Shenzhen) in 2014 and 2018 respectively. Now he as is currently a postdoctoral researcher at the School of Advanced Materials, Peking University Shenzhen Graduate School (China) in Prof. Feng Pan's group. His research interests are energy storage and conversion.

**Weiyuan Hang** received his B.S. degree in New Energy Materials and Devices from South China Normal University in 2017. He is pursuing his M.S. degree in the School of Advanced Materials, Peking University, China. His research interest is energy storage and conversion applications including lithium ion batteries, sodium ion batteries, and super capacitors.

**Aoye Song** graduated with a B.S. degree in the College of Chemistry and Molecular Engineering of Peking University (PKU, China) in 2018. He is now pursuing a master's degree with Prof. Feng Pan at the School of Advanced Materials, Peking University Shenzhen Graduate School, China. His main research interests are advanced energy storage materials, including sodium ion batteries, zinc-ion aqueous batteries.

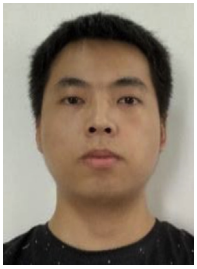

**Yuetao Wang** graduated from Peking Univerisity (PKU,China) and received his Bachelor's Degree from the College of Chemistry and Molecular Engineering in 2018. Wang is now studying for a Ph.D degrees under the leadership of Prof. Feng Pan at the School of Advanced Materials, Peking University Shenzhen Graduate School, China. He mainly focused on the research of aqueous battery systems, especially on the zinc-ion batteries and the zinc anode materials.

**Shouxiang Ding** majored in Chemical Engineering and received his bachelor degree of engineering from the School of Chemistry and Chemical Engineering at South China University of Technology (SCUT, China) in June 2019. Shouxiang Ding is admitted as a master student by the School of Advanced Materials with Prof. Feng Pan at the Peking university. His research interests focus on the cathode materials of aqueous zinc ion battery.

**Yongli Song** was born in Harbin, China. He received the B.S. degree (2010) in Optics and the M.S. degree (2013) in Condensed Matter Physics from Harbin Institute of Technology (HIT), China. In 2017, he received his Ph.D. degree in Prof. Y. Sui's group at the department of physics, HIT. He is now working as a postdoctoral researcher in Prof. F. Pang group. His current research is focused on lithium-based batteries.

**Guoyu Qian** received his Ph.D. from Huazhong University of Science and Technology in 2018 and was at Columbia University as a joint Ph.D. student in 2016–2017. He is currently a postdoctoral scholar at Peking University Shenzhen Graduate School. His research interests focus on studies of lithium-ion batteries, flexible energy storage and multiferric materials.

**Haibiao Chen** is currently a senior researcher at the School of Advanced Materials, Peking University Shenzhen Graduate School. He received his Bachelor's degree from Tsinghua University in 2000 and PhD from Stevens Institute of Technology in 2006. He worked at Velocys during 2006–2011 and UES during 2011–2014 prior to joining Peking University Shenzhen Graduate School.

**Feng Pan,** Chair-Professor, Founding Dean of School of Advanced Materials, Peking University Shenzhen Graduate School, Director of National Center of Electric Vehicle Power Battery and Materials for International Research, got B.S. from Dept. Chemistry, Peking University in1985 and PhD from Dept. of P&A Chemistry, University of Strathclyde, Glasgow, UK, with “Patrick D. Ritchie Prize” for the best Ph.D. in 1994. Prof. Pan has been engaged in fundamental research and product development of novel energy conversion and storage materials & devices. As Chief Scientist, Prof. Pan led 12 entities to win National Key project of Material Genomic Engineering for Solid State Li-ion Battery in China in 2016. He has been selected as one of the 2018 winner of ECS Battery Division Technology Award.